ACS OMEGA

http://pubs.acs.org/journal/acsodf

Article

Influence of Temperature on ZnO/Co_3O_4 Nanocomposites for High Energy Storage Supercapacitors

Eshetu M. Abebe and Masaki Ujihara*

Cite This: *ACS Omega* 2021, 6, 23750−23763

Read Online

ACCESS | Metrics & More | Article Recommendations | Supporting Information

ABSTRACT: We developed a two-step chemical bath deposition method followed by calcination for the production of ZnO/Co_3O_4 nanocomposites. In aqueous reactions, ZnO nanotubes were first densely grown on Ni foam, and then flat nanosheets of Co_3O_4 developed and formed a porous film. The aspect ratio and conductivity of the Co_3O_4 nanosheets were improved by the existence of the ZnO nanotubes, while the bath deposition from a mixture of Zn/Co precursors (one-step method) resulted in a wrinkled plate of Zn/Co oxides. As a supercapacitor electrode, the ZnO/Co_3O_4 nanosheets formed by the two-step method exhibited a high capacitance, and after being calcined at 450 °C, these nanosheets attained the highest specific capacitance (940 F g^{-1}) at a scan rate of 5 mV s^{-1} in the cyclic voltammetry analysis. This value was significantly higher than those of single-component electrodes, Co_3O_4 (785 F g^{-1}) and ZnO (200 F g^{-1}); therefore, the presence of a synergistic effect was suggested. From the charge/discharge curves, the specific capacitance of ZnO/Co_3O_4 calcined at 450 °C was calculated to be 740 F g^{-1} at a current density of 0.75 A g^{-1}, and 85.7% of the initial capacitance was retained after 1000 cycles. A symmetrical configuration exhibited a good cycling stability (Coulombic efficiency of 99.6% over 1000 cycles) and satisfied both the energy density (36.6 Wh kg^{-1}) and the power density (356 W kg^{-1}). Thus, the ZnO/Co_3O_4 nanocomposite prepared by this simple two-step chemical bath deposition and subsequent calcination at 450 °C is a promising material for pseudocapacitors. Furthermore, this approach can be applied to other metal oxide nanocomposites with intricate structures to extend the design possibility of active materials for electrochemical devices.

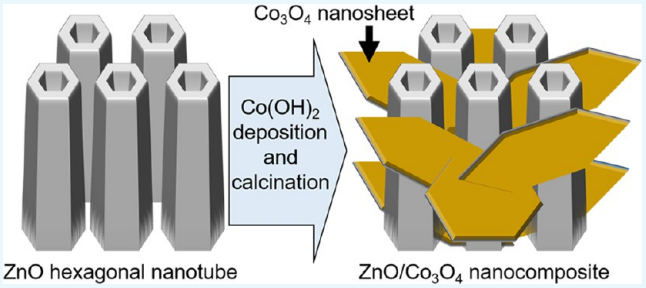

INTRODUCTION

Currently, energy sources such as solar energy and wind energy have been receiving considerable attention worldwide because they are renewable and pollution-free.[1] To use these energy sources in practice, energy storage and conversion technologies play a significant role. Li-ion batteries (LIBs), supercapacitors, water splitting, CO_2 reduction, and fuel cells are typical electrochemical systems for energy storage and conversion technologies. In these systems, materials and structures are crucial. Electrode materials with high activity, large surface area, and sufficient durability are commonly required for both effective energy storage and energy conversion.[2,3] Since the activity of materials depends on the applications, various materials have been examined as electrode materials for LIBs,[4] as catalysts for the hydrogen evolution reaction (HER),[5−7] and the oxygen evolution reaction (OER)[8] in water splitting.[9] Electrodes have also been developed for supercapacitors. Supercapacitors, also known as ultracapacitors or electrochemical capacitors, are advanced electronic devices that store and release bulk electrical energy with a charge separation between the electrolyte and the surface of nanostructured electrodes.[10] Supercapacitors are expected to be promising energy storage devices due to their high specific power, compact size, a wide range of operating temperatures, and excellent cycling stability.[11−15] However, the energy density of supercapacitors is considerably lower than that of batteries.[16] To increase their energy density, several derivatives have been developed. Depending on the energy storage mechanisms, they can be categorized into three categories: electrochemical double-layer capacitors (EDLCs, nonfaradic), pseudocapacitors (faradic, redox-based electrochemical capacitors), and hybrid capacitors, which consist of a nonfaradic electrode and a faradic electrode.[17,18] Among these, EDLCs especially have a high specific power density, fast charge/discharge rates, long cycle life, and environmental friendliness,[18,19] while pseudocapacitors have a higher capacitance and energy density than EDLCs.[20,21] The surface area of electrodes is commonly a crucial factor that facilitates ion adsorption/desorption, while electrode materials in the pseudocapacitors should be designed to allow sufficient redox reactions.[22]

Received: April 17, 2021
Accepted: August 6, 2021
Published: September 8, 2021

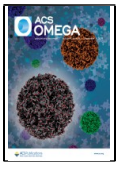

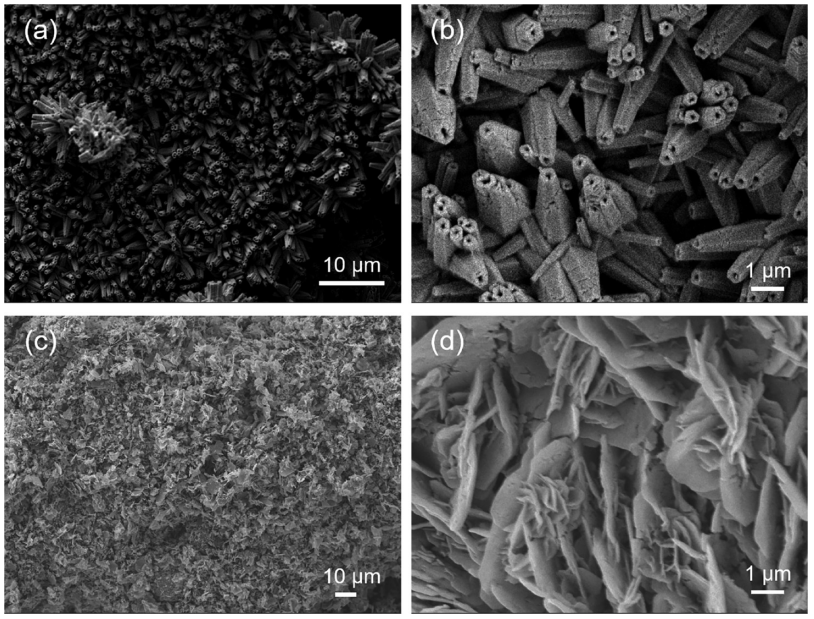

Figure 1. Scanning electron microscope(SEM) images of (a and b) ZnO and (c and d) Co_3O_4@450.

As electrode materials for supercapacitors, carbon materials, conducting polymers (CPs), and transition metal oxides (TMOs) have been widely studied.[23−26] Among them, TMOs have been intently studied as pseudocapacitors because of their stable redox reactions and high specific capacitance.[27−29] Since the characteristics of TMOs depend on their metal species, a variety of TMOs has been designed to improve performance. TMOs could be hybridized with the other materials to improve the electrochemical performances of a supercapacitor: e.g., carbon materials can be used to extend the surface area and introduce a conductive path to TMOs, and conductive polymers can mechanically support the TMO.[27−29] The effects of hybridization can appear additively, synergistically, or destructively. Therefore, the combination of materials and the preparation procedures have been carefully considered to optimize the electrode performance. The hybridization between TMOs is also performed in anticipation of synergistic effects: complicated structures with a large surface area can be formed, electric resistance can be reduced by the introduction of the conductive path, and the redox potential can be controlled by effective charge transfer. Anticipating these synergistic effects, various nanocomposites of different TMOs, such as WO_3/TiO_2,[30] $Co_3S_4@Co_3O_4$,[31] ZnO−NiO,[32] and $ZnCo_2O_4@MnCo_2O_4$,[33] have been reported. To design the structures, metal−organic frameworks (MOFs) and TMOs derived from the MOFs are also reported.[34,35] In particular, Co_3O_4 is an attractive hybrid component candidate because of its low cost, natural abundance, environmental friendliness, structures with high surface area, high redox activity, and high theoretical capacitance (approximately 3560 F g^{-1}).[18,19,36] On the other hand, ZnO is also a promising candidate for supercapacitor applications due to its environmental friendliness, low cost, biocompatibility, high electrical conductivity, and excellent chemical and thermal stabilities.[19,37] Moreover, since ZnO is among the best semiconductor materials, its capacitance contribution is less, so the ZnO layer can be used as a powerful mechanical support for redox materials and offers a sufficient pathway for the electron transport of the electrode materials due to its high mechanical flexibility and chemical stability in alkaline and neutral electrolytes.[38,39]

For electrode preparation, Co_3O_4 and its composite materials are mostly provided in powder form and then mixed with other conductive materials and binders to be placed as a slurry on current collectors.[40] The Co_3O_4 powder is synthesized by a hydrothermal method, which is a difficult process that requires a high temperature and pressure. Furthermore, during the mixing process, the use of conductive additives and polymer binders results in the degradation of nanostructures and blocking of electroactive surfaces, thus decreasing the electron transfer ratio and ion diffusion.[41] To enhance the electrochemical performance of the electrode, direct growth of ZnO/Co_3O_4 nanocomposites on conducting current collectors, which avoided the use of a binder and a tedious process, will be more applicable since every nanostructure having electrical contact with current collectors reduces the internal resistance.

In this study, we developed a two-step chemical bath deposition (CBD) method that was easy, economical, convenient, and highly reproducible. The Co_3O_4 and ZnO/Co_3O_4 nanocomposites were directly grown on a Ni foam current collector without a binder, and the effect of calcination temperature was investigated. Herein, we designed a porous film of ZnO/Co_3O_4 nanosheets synthesized by a two-step CBD method, and the structures and electrochemical performance were analyzed as an electrode material for pseudocapacitors. The electrode material, which is prepared directly on Ni foam current collectors using the CBD method without polymer binders, could provide a high surface area, stable structure, and favorable kinetics, which ought to enhance the electroactive sites and electrochemical performance.

RESULTS AND DISCUSSION

Morphological and Structure Characterization. Ni foam has been widely used as a current collector due to its high conductivity, uniform macropores, large surface area, and ability to support a high loading of the active material.[42,43] ZnO, Co_3O_4, $ZnO@Co_3O_4$, and ZnO/Co_3O_4 are active

https://doi.org/10.1021/acsomega.1c02059
ACS Omega 2021, 6, 23750−23763

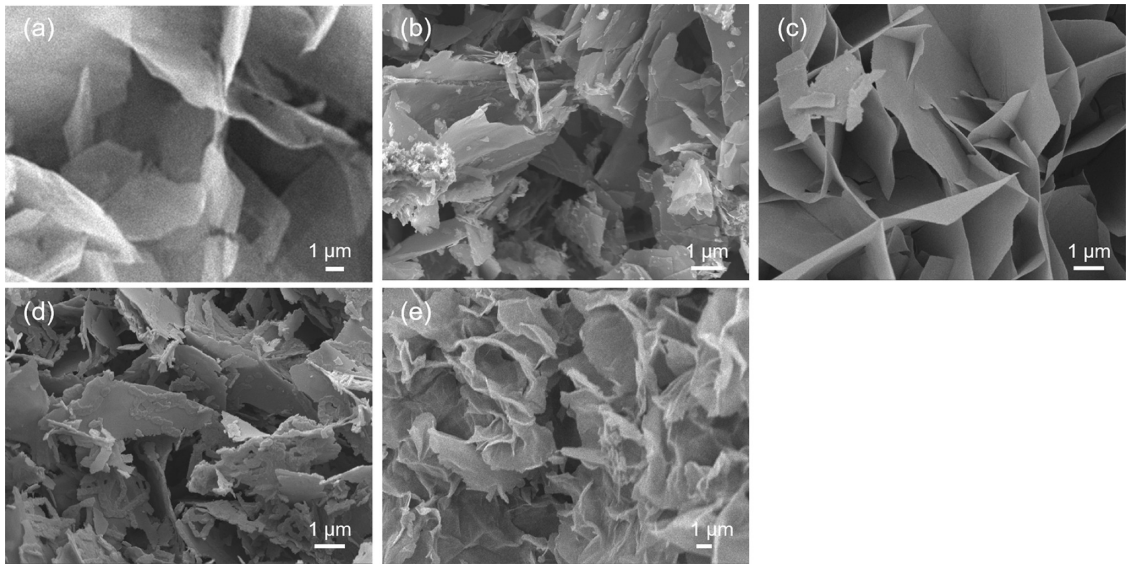

Figure 2. SEM images of ZnO/Co_3O_4 calcined at (a) 250 °C, (b) 350 °C, (c) 450 °C, and (d) 550 °C and (e) $ZnO@Co_3O_4$ calcined at 450 °C.

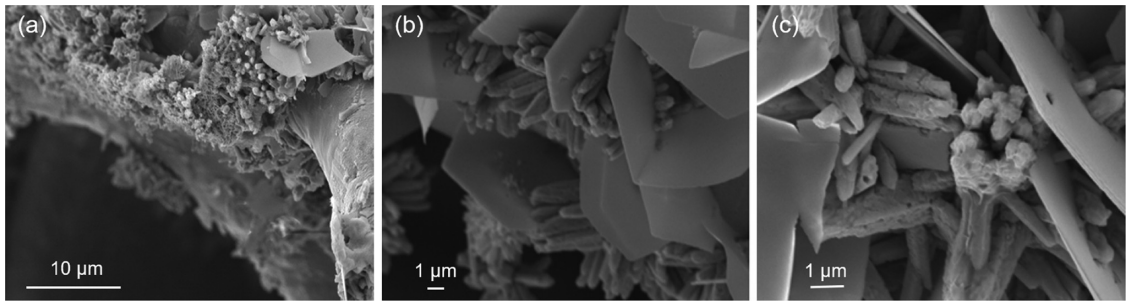

Figure 3. Cross-sectional SEM images of ZnO/Co_3O_4@450 at (a) low magnification and (b, c) high magnification.

materials for supercapacitors, and their direct growth on Ni foam via the CBD method followed by heat treatment at different temperatures (250, 350, 450, and 550 °C) was studied to understand the growth of their structures. The samples were named according to the chemical components and calcination temperature used for their synthesis (ZnO/Co_3O_4@250 ZnO/Co_3O_4@350, ZnO/Co_3O_4@450, Co_3O_4@450, and ZnO/Co_3O_4@550).

First, the nanostructures of the individual components (ZnO and Co_3O_4@450) were observed (Figure 1). ZnO was deposited on the Ni foam using a CBD method previously reported with slight modifications.[44] As observed, ZnO hexagonal nanotubes (HNTs) were formed with an average thickness, length, and diameter of 76 nm, 1.36 μm, and 262 nm, respectively (Figure 1a,b). In contrast, the Co_3O_4 developed a nanosheet array that uniformly covered the Ni foam after calcination at 450 °C (Figure 1c,d) using a previously reported method.[45] The average length and thickness of each Co_3O_4 nanosheet were approximately 1.16 μm and 86 nm, respectively. These structures were highly porous, which is suitable for electrolyte diffusion.

Next, the ZnO/Co_3O_4 nanocomposites were prepared through three steps: ZnO HNTs, $Co(OH)_2$ deposition, and calcination. Calcination was applied to partially oxidize Co^{2+} to Co^{3+} and develop a crystal structure. The oxidation of Co ions was confirmed by observing the color change from green (before calcination) to black (after calcination). SEM images revealed that the morphologies of the ZnO/Co_3O_4 nanocomposites were nanosheet arrays (Figure 2).

The average length and thickness of each nanosheet in ZnO/Co_3O_4@450 were 1.74 μm and 48 nm, respectively, which were significantly longer and thinner than those of Co_3O_4@450 (1.16 μm and 86 nm). This change could be induced by the existence of Zn ions in the $Co(OH)_2$ deposition: in the reaction solution of $Co(OH)_2$ deposition, the ZnO partially dissolved in the solution due to the ammonia released from urea. The Zn ions were adsorbed onto the $Co(OH)_2$ crystal and controlled its growth direction to a high aspect ratio.[46,47] In contrast, the $ZnO@Co_3O_4$@450 obtained from the Zn/Co precursor mixture by one-step bath deposition had an average thickness of ∼97 nm, which was thicker than that of ZnO/Co_3O_4@450 (Figure 2d). The nanosheets of $ZnO@Co_3O_4$@450 were also wrinkled and not orderly aligned on the Ni foam substrate, which could be due to the lattice mismatch of $Co(OH)_2$ and ZnO crystals during nucleation and crystal growth in the deposition process; furthermore, $Co(OH)_2$ likely forms a layered structure, while ZnO forms a columnar crystal.[48,49] The different morphologies and sizes of these nanocomposites demonstrated the necessity of the separated deposition of Zn and Co. ZnO/Co_3O_4@450 with an interconnected porous morphology and a large surface area was expected to be advantageous for application in pseudocapacitors.[50] The morphology difference in the ZnO/Co_3O_4 nanostructure is evidence of an effect of calcination temperature. Figure 2a clearly indicates that flat nanosheets

https://doi.org/10.1021/acsomega.1c02059
ACS Omega 2021, 6, 23750−23763

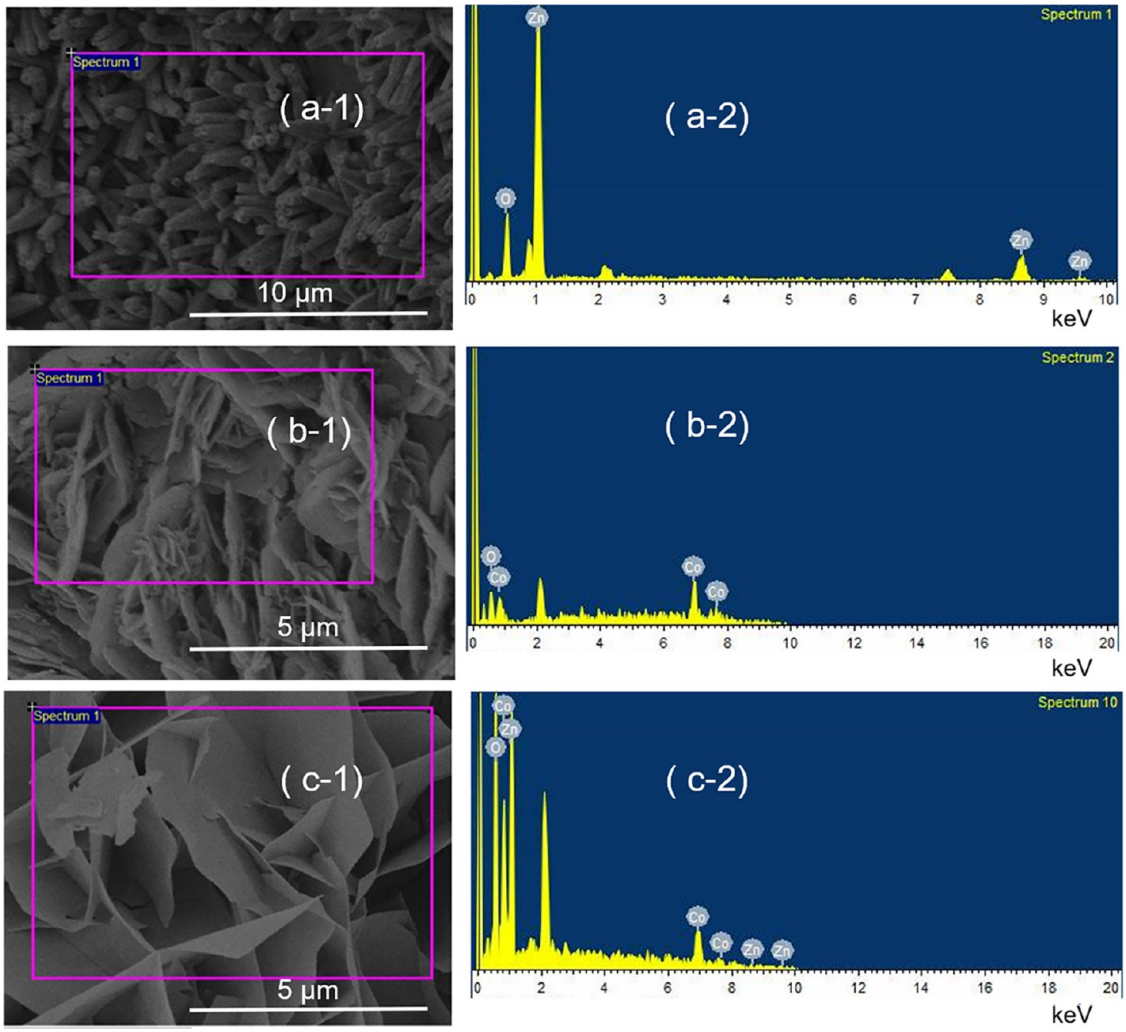

Figure 4. SEM images of synthesized (a-1) ZnO, (b-1) Co_3O_4@450, and (c-1) ZnO/Co_3O_4@450 electrodes; and their energy dispersive spectroscopy (EDS) spectra (a-2, b-2, and c-2), respectively.

were formed when the sample was calcined at 250 °C. After the application of different calcination temperatures, ZnO/Co_3O_4@350 developed nanosheets with an average length and thickness of approximately 1.45 μm and 67 nm, respectively. Additionally, ZnO/Co_3O_4@550 had many voids in the nanosheets. These changes in the thickness and the number of defects suggested that calcination at high temperature resulted in thermal decomposition of nanocomposites, including the dehydration of the remaining metal hydroxides and the thermal reduction of metal oxides, thus leading to thinner films with more defects.

In Figure 2a−d, ZnO HNTs were not observed. Subsequently, the cross section of the Ni foam after the deposition of ZnO/Co_3O_4@450 was observed (Figure 3). The inner wall of the Ni foam was homogeneously covered by the nanocomposites (Figure 3a), while the ZnO HNT structure was retained. The ZnO HNTs on outermost surface were covered by nanosheets, and therefore not observed in Figure 2a−d. The outer wall of the Ni foam was exposed to the reaction solution, and therefore, more $Co(OH)_2$ deposition occurred on the outer surface to cover the ZnO HNTs than the inside of the foam. In detail, the ZnO HNTs were covered by ultrathin Co_3O_4 films, which evenly spread out on the large nanosheets (Figure 3b). Furthermore, the surface of ZnO HNTs seems to be corroded (Figure 3c), which suggests that the Zn ions eluted from the ZnO HNTs during the $Co(OH)_2$ deposition. These structures supported the hypothesis of a thin nanosheet growth mechanism: in the vicinity of ZnO, the concentration of Zn ions became higher, and thus the deposition of $Co(OH)_2$ in the thickness direction was strongly regulated.[47,51]

To confirm the coexistence of Zn and Co oxides in the nanocomposite, elemental analyses were also performed (Figure 4).

The ZnO HNTs showed the existence of Zn and O with a small amount of Ni from the substrate. The EDS elemental analysis of Co_3O_4@450 indicated the existence of Co and O with a ratio of 2.75:3.91; this experimental ratio was consistent with the theoretical ratio of 3:4 with a slight excess of oxygen due to the remaining OH groups. Moreover, the EDS spectrum of ZnO/Co_3O_4@450 demonstrated the presence of Zn, Co, and O with elemental ratios of 13.36% for Zn, 32.19% for Co, and 54.45% for O. Assuming that all of the Zn ions were bound with O as ZnO, the ratio of Co to O was 32:41, which was consistent with the expected formation of Co_3O_4. To know the distribution of elements, the EDS elemental mapping of the ZnO/Co_3O_4@450 nanosheet structure was further conducted. The elements, Zn, Co, and O were

https://doi.org/10.1021/acsomega.1c02059
ACS Omega 2021, 6, 23750−23763

uniformly distributed throughout the nanosheets (Figure S1 in the supporting information).

Next, the structural properties and crystal phases of Co_3O_4@450 and ZnO/Co_3O_4 calcined at different temperatures from 250 to 550 °C were analyzed using X-ray diffraction (XRD) (Figure 5). The three sharp diffraction peaks at 2θ of 44.27,

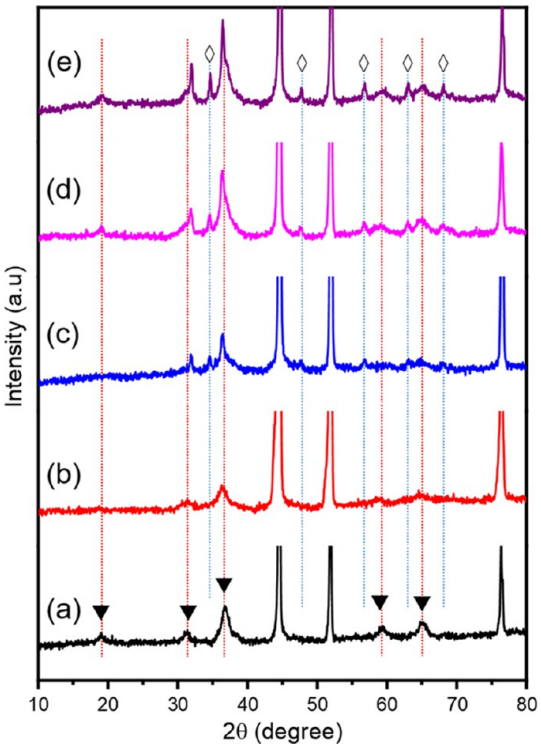

Figure 5. XRD charts of (a) Co_3O_4 @450 and ZnO/Co_3O_4 calcined at (b) 250, (c) 350, (d) 450, and (e) 550 °C. Each peak was marked by symbols (◊ for ZnO and ▼ for Co_3O_4) and dotted lines.

51.87, and 76.31° were attributed to the lattice planes of (111), (200), and (220) of the Ni foam substrate, respectively (JCPDS-2865). The peaks at 19.07, 31.32, 36.84, 59.36, and 65.24° were commonly observed in both materials and corresponded to the (111), (220), (311), (511), and (440) lattice planes of the cubic spinel phase of Co_3O_4 (JPPDS no. 42-1467), respectively. The XRD spectra of ZnO/Co_3O_4@450 exhibited additional peaks at 34.67, 47.61, 56.72, 62.75, and 68.17°, which were indexed to the (002), (102), (110), (103), and (112) lattice planes of hexagonal ZnO, respectively. The presence of both ZnO and Co_3O_4 structures suggested that these two metal oxides separately existed in the nanocomposite, as shown by the SEM images (Figure 3). The diffraction peaks of ZnO/Co_3O_4@450 were broader than those of Co_3O_4@450, which verified that it had smaller crystal grains.[52] As the calcination temperature was increased from 250 to 550 °C, the intensity and sharpness of the diffraction peaks of ZnO/Co_3O_4 increased, which suggests that the crystallization of ZnO/Co_3O_4 progressed at higher temperature.[53,54] Using the Scherrer equation (eq 1),[55] the mean crystal grain size of nanocomposites was calculated

$$D = K\lambda/\beta \cos\theta \quad (1)$$

where D is the crystallite size (nm), K = 0.9 (Scherrer constant), λ = 0.15406 nm (wavelength of the X-ray source), β is the full width at half-maximum (FWHM, radians), and θ is the peak position (radians). The mean crystal grain sizes of Co_3O_4@450, ZnO/Co_3O_4@250, ZnO/Co_3O_4@350, ZnO/Co_3O_4@450, and ZnO/Co_3O_4@550 were, respectively, calculated to be 9.0, 5.2, 6.5, 7.0, and 8.2 nm, which confirmed the progress of crystallization by the high temperature and the regulation by the Zn ions.

To further characterize the metal oxides, Fourier transform infrared (FTIR) spectra of Co_3O_4@450 and ZnO/Co_3O_4@450 were obtained (Figure 6). The broad bands at 3433 and

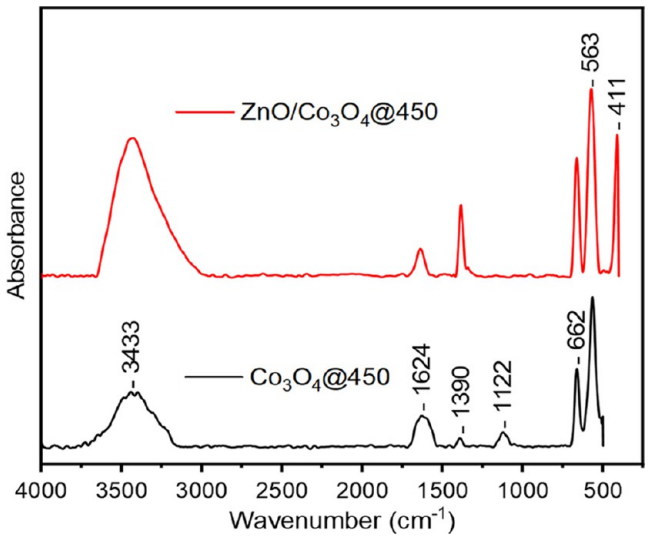

Figure 6. FTIR absorption spectra of Co_3O_4@450 and ZnO/Co_3O_4@450.

1624 cm^{-1} observed in Co_3O_4@450 were assigned to the O−H stretching and bending vibrational modes, respectively.[56] The bands at 1390 and 1122 cm^{-1} in Co_3O_4@450 were attributed to the stretching vibrations of residual NO_3^- and the bending vibrations of −OH groups bound to Co ions, respectively.[57,58] The bands observed at 662 and 563 cm^{-1} were associated with the stretching vibrations of Co^{2+}−O and Co^{3+}−O bonds in the spinel cobalt oxide, respectively, thereby showing the presence of crystalline Co_3O_4.[59] A new band at 411 cm^{-1} in ZnO/Co_3O_4@450 was associated with ZnO.[60] Thus, the coexistence of the Co_3O_4 and ZnO crystals was confirmed from both the XRD and FTIR analyses.

To further investigate the chemical states, the nanocomposites were analyzed using X-ray photoelectron spectrometry (XPS). The survey XPS spectra of the ZnO/Co_3O_4 calcined at different temperatures (250, 350, 450, and 550 °C) and the ZnO@Co_3O_4@450 clearly indicated the existence of O, Co, and Zn (Figure S2 in the supporting information). The high-resolution XPS spectra of Zn 2p, Co 2p, and O 1s are shown in Figure 7. The Zn 2p spectra exhibited two symmetric peaks: the binding energy of Zn $2p_{3/2}$ was around 1022 eV, while the peak of Zn $2p_{1/2}$ appeared around 1045 eV. As the temperature increased, the Zn 2p peaks shifted toward a lower energy, but the energy difference between the Zn $2p_{3/2}$ and Zn $2p_{1/2}$ was approximately 23 eV, which indicates the existence of Zn^{2+} in the nanocomposite.[61] The Co 2p spectra consisted of two spin−orbit doublets around 780 and 795 eV, which were, respectively, assigned to Co^{2+} and Co^{3+}. The area ratios of Co^{3+}/Co^{2+} in ZnO/Co_3O_4 nanocomposites calcined at 250, 350, 450, and 550 °C were 0.56, 0.67, 0.92, and 0.54, respectively. The ratio of Co^{3+}/Co^{2+} increased as the

https://doi.org/10.1021/acsomega.1c02059
ACS Omega 2021, 6, 23750−23763

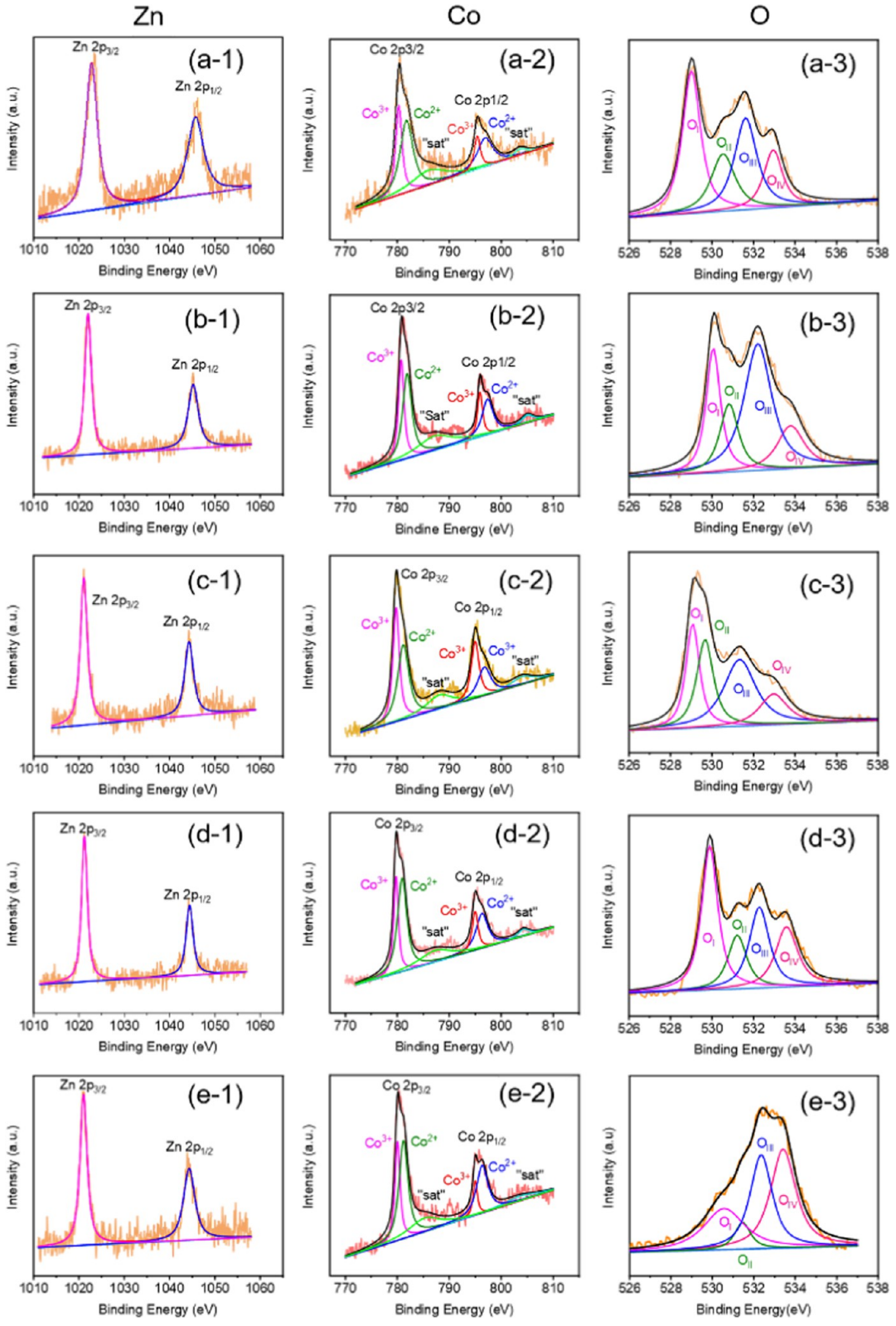

Figure 7. XPS spectra of ZnO/Co_3O_4 nanocomposites calcined at the temperatures of 250 °C (a-1 to a-3), 350 °C (b-1 to b-3), 450 °C (c-1 to c-3), 550 °C (d-1 to d-3), and $ZnO@Co_3O_4@450$ (e-1 to e-3), respectively. The two minor shakeup satellites are denoted as "sat" in Co 2p spectra.

calcination temperature was increased from 250 to 450 °C, which indicates that oxidation of Co ions progressed. However, the Co^{3+}/Co^{2+} ratio in $ZnO/Co_3O_4@550$ decreased, which could be due to the partial decomposition of Co_3O_4 to CoO (see Figure 2).[62] The O 1s spectra of ZnO/Co_3O_4 nanocomposites consisted of four peaks. Peaks around 530 and 531 eV were assigned to the metal−oxygen bond (O_I) and oxygen vacancies (O_{II}), respectively. The peaks at higher binding energies (O_{III} and O_{IV} around 532 and 533 eV, respectively) were attributed to the defects and the absorbed oxygen species

https://doi.org/10.1021/acsomega.1c02059
ACS Omega 2021, 6, 23750−23763

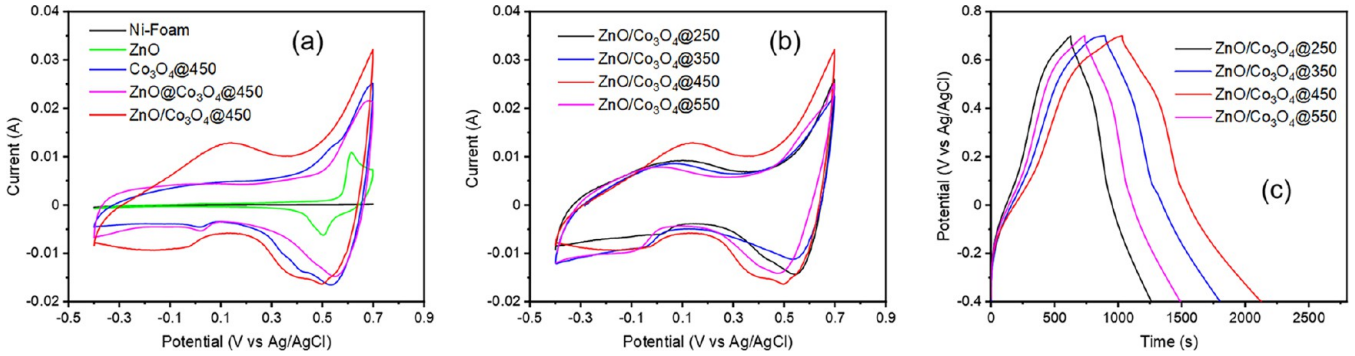

Figure 8. (a) CV curves of the different electrodes measured at 5 mV s^{-1}, (b) CV curves of ZnO/Co_3O_4 calcined at different temperatures, and (c) GCD curves of ZnO/Co_3O_4 calcined at different temperatures and measured at 0.75 A g^{-1}.

(e.g., O_2, H_2O, and carbonates).[63] Although O_I and O_{II} could originate from both of Co and Zn, the relative concentrations of oxygen-deficient centers in the nanocomposites were estimated from the ratios of O_{II}/O_I.[64] From the XPS peak areas, the ratios of O_{II}/O_I were 0.5, 0.7, 0.91, and 0.43 for ZnO/Co_3O_4 calcined at 250, 350, 450, and 550 °C, respectively. This suggests that the thermal decomposition of metal oxides to generate the oxygen vacancies progressed as the calcination temperature increased, and the restructuring of oxygen-deficient Co_3O_4 to CoO occurred in the nanocomposite of ZnO/Co_3O_4@550.[62] In comparison to ZnO/Co_3O_4@450, the $ZnO@Co_3O_4$@450 exhibited a significantly lower oxygen-deficient ratio (O_{II}/O_I = 0.25), and the O_I peak was much broader. These differences could be explained by the involved structure of the $ZnO@Co_3O_4$@450, as seen in Figure 2.

Electrochemical Performance Analysis. All of the synthesized electrode materials were electrochemically characterized by the cyclic voltammetry (CV) and galvanostatic charge/discharge (GCD) methods (Figure 8). The typical CV curves of the bare Ni foam, ZnO HNTs, Co_3O_4@450, $ZnO@Co_3O_4$@450, and ZnO/Co_3O_4@450 samples at a scan rate of 5 mV s^{-1} in the potential range from −0.4 to 0.7 V vs Ag/AgCl are shown in Figure 8a. The contribution of Ni foam to the total capacitance was almost negligible, and the observed peaks in each curve demonstrated the pseudocapacitive properties of each material. The mass of the active material loaded on the current collector was 1.8 mg for ZnO, 4.6 mg for Co_3O_4, and 5.5 mg for ZnO/Co_3O_4. The specific capacitance (C_{sc}) was then calculated. ZnO/Co_3O_4@450 had a C_{sc} of 940 F g^{-1}, which was greater than the C_{sc} values of Co_3O_4@450 (785 F g^{-1}) and ZnO HNTs (200 F g^{-1}), thus suggesting that these materials exhibited a synergistic effect. This synergistic effect strongly appeared with the oxidation wave at 0.14 V and the broad reduction wave between −0.04 and −0.4 V (centered at −0.18 V), which were not observed with the other materials and indicate new redox potentials formed by the hybridization. The C_{sc} of $ZnO@Co_3O_4$@450 was 650 F g^{-1}, which was lower than the C_{sc} values of Co_3O_4@450 and ZnO/Co_3O_4@450, as expected from the disordered structure of $ZnO@Co_3O_4$@450 (Figure 2d). Notably, the redox waves at 0.14/−0.18 V were not observed in $ZnO@Co_3O_4$@450. That is, the coprecipitation of Zn and Co oxides from the mixed precursors decreased the synergistic effect. Furthermore, the synergistic effect was not from the doping of Zn ions in the crystal lattice of Co_3O_4 because the excess Zn ions could block the active sites in the Co oxide.[18]

To confirm the effects of the calcination temperature, CV measurements were conducted for ZnO/Co_3O_4 calcined at different temperatures (Figure 8b). The synergistic effect was prominent in ZnO/Co_3O_4@450, which exhibited a larger CV curve area than the others. The specific capacitance (C_{sc}) values of ZnO/Co_3O_4@250, ZnO/Co_3O_4@350, ZnO/Co_3O_4@450, and ZnO/Co_3O_4@550 were 714, 850, 940, and 800 F g^{-1}, respectively, at 5 mV s^{-1}. The largest C_{sc} of ZnO/Co_3O_4@450 could be explained by the expected high aspect ratio and decreased number of defects in the nanostructures (see Figure 2).[65]

Moreover, changes in redox waves were found to enhance the capacitance. Commonly, a single oxidation wave (∼0.14 V) and two reduction waves (0.4−0.6 V and approximately −0.18 V) were found in the CV curves of the ZnO/Co_3O_4 nanocomposites, which could be attributed to the redox reactions of $Co_3O_4/CoOOH/CoO_2$.[18] Focusing on the reduction wave at 0.4−0.6 V, ZnO/Co_3O_4@250 and ZnO/Co_3O_4@350 exhibited a reduction wave at 540 mV, which was higher than the waves in ZnO/Co_3O_4@450 (490 mV) (Figure 8a). This result suggested that the calcination of Co_3O_4 was not achieved at 250−350 °C. Additionally, ZnO/Co_3O_4@550 shifted this wave to an even lower potential (470 mV). Therefore, ZnO/Co_3O_4@450 provided both characteristics associated with a slight shift toward a lower potential (center was at 500 mV). These waves were associated with the reduction of Co ions, which appeared at 530 mV in Co_3O_4@450 (Figure 8a). The shifts of the reduction wave to lower potentials suggest that the materials became less active in the reduction reactions. The high crystallinity could stabilize the materials toward the redox reactions in this range, while the current intensity was supported by the surface area of the materials. $ZnO@Co_3O_4$@450 with disordered structures (Figure 2e) exhibited the wave at the highest potential (550 mV), which suggested that similar to ZnO/Co_3O_4@250 and ZnO/Co_3O_4@350, the crystalline structures were not developed in this nanocomposite.

For the waves that appeared by the synergistic effects (0.14 and −0.18 V), both waves exhibited a similar change in their potential: calcination at 450 °C provided the highest potential, followed by calcination at 350 °C. The mechanism of this shift was not clear and would be helpful in designing synergistic effects in the future.

Figure 8c represents the GCD curves of ZnO/Co_3O_4 calcined at different temperatures measured at a current density of 0.75 A g^{-1}. The GCD curves of these materials were not ideally linear, which could be attributed to redox

https://doi.org/10.1021/acsomega.1c02059
ACS Omega 2021, 6, 23750−23763

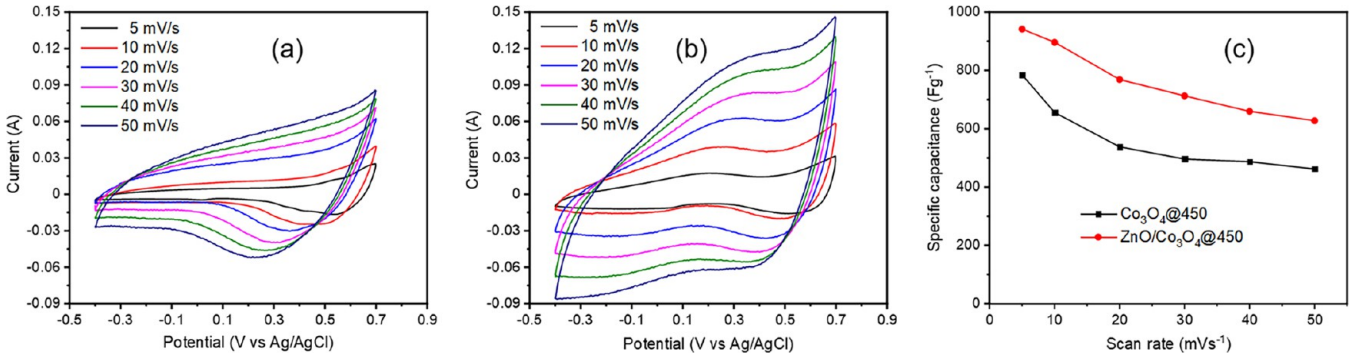

Figure 9. CV curves of (a) Co_3O_4@450 and (b) ZnO/Co_3O_4@450 at different scan rates and the (c) specific capacitance vs scan rate plots.

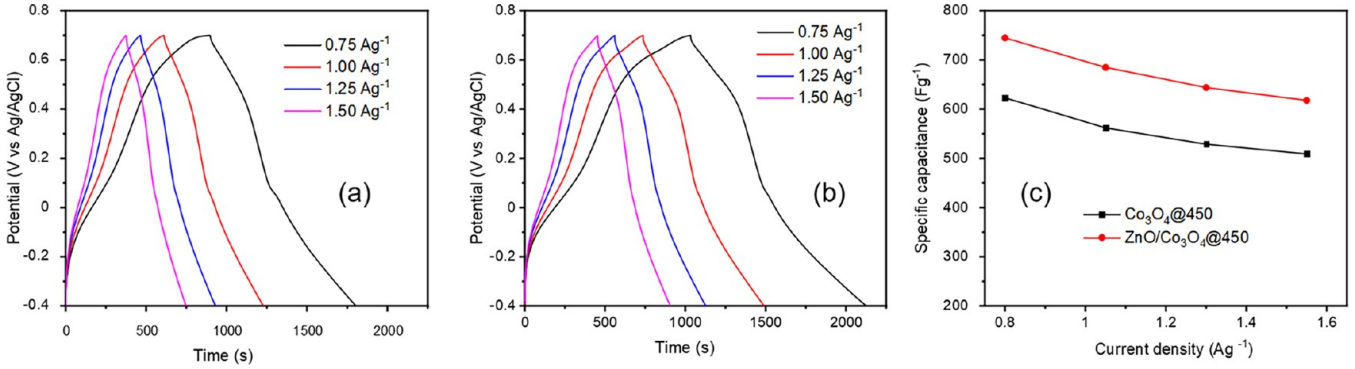

Figure 10. GCD curves of (a) Co_3O_4@450 and (b) ZnO/Co_3O_4@450 at different current densities and the (c) specific capacitance vs current density plot.

reactions,[66] as shown in the CV curves. The specific capacitance values (C_{sg}) of ZnO/Co_3O_4@250, ZnO/Co_3O_4@350, ZnO/Co_3O_4@450, and ZnO/Co_3O_4@550 were calculated to be 430, 610, 740, and 510 F g^{-1}, respectively, which were consistent with those of the CV measurement results, although the C_{sg} values were smaller than the corresponding C_{sc} values because of differences in the current density and scan ratio. At the high calcination temperature of 550 °C, the specific capacitance decreased due to a loss in the hydrous content of cobalt oxide[54] and could be due to structural deformation, which decreased the effective surface area and increased the electrical resistance.

CV measurements were also performed at different scan rates from 5 to 50 mV s^{-1} to test the kinetic behavior of Co_3O_4 and ZnO/Co_3O_4@450 (Figure 9a,b).

ZnO/Co_3O_4@450 exhibited a higher capacitance than Co_3O_4@450 at all scan rates. As the scan rate increased from 5 to 50 mV s^{-1}, the anodic peaks for ZnO/Co_3O_4@450 shifted toward a more positive potential, while the cathodic peaks shifted toward a more negative potential, suggesting that ion diffusion limited the redox reactions.[67] As a result of electrolyte diffusion in the active material, the specific capacitance decreased at high scan rates (Figure 9c). When the scan rate increased to 50 mV s^{-1}, the specific capacitances of Co_3O_4@450 and ZnO/Co_3O_4@450 decreased to 462 and 630 F g^{-1}, and their capacitance retention was 59 and 67% of the specific capacitance at 5 mV s^{-1}, respectively, which indicates that ZnO/Co_3O_4@450 has a higher rate capability than Co_3O_4@450.

The kinetics was also analyzed from the GCD curves (Figure 10a,b). The nonlinear GCD curves suggested that the redox reactions of Co ions[66] were consistent with the CV curves. The discharging time of ZnO/Co_3O_4@450 was longer than that of Co_3O_4@450, indicating that ZnO/Co_3O_4@450 had a higher specific capacitance. The C_{sg} values of ZnO/Co_3O_4@450 were 740, 690, 640, and 620 F g^{-1} at current densities of 0.75, 1.00, 1.25, and 1.50 A g^{-1}, respectively, while those of Co_3O_4@450 were 620, 560, 530, and 510 F g^{-1}, respectively (Figure 10c). As the current density increased, the specific capacitance of the materials decreased, which could be attributed to the decrease in the effective surface area in contact with the electrolyte: the diffusion layer became too thick to ignore the small pores in the nanocomposites. Considering the microporous structure of the Ni foam, the inhomogeneous flow of the electrolyte between the skin and the inner spaces of the electrode could also cause a decrease in the specific capacitance at a high current density.

To analyze the details of the electrochemical behaviors, electrochemical impedance spectroscopy (EIS) measurements were performed on the Co_3O_4 and ZnO/Co_3O_4 nanocomposites (Figure 11).

The Nyquist plots, where Z' and Z'' are the real and imaginary impedances, respectively, for both nanocomposites exhibited small semicircles in the high-frequency region and positively sloped curves in the low-frequency region. In the high-frequency region, ZnO/Co_3O_4@450 showed the smallest semicircle diameter, which suggested the lowest resistance in the charge transfer process. According to the equivalent circuit model (inset in Figure 11), the charge transfer resistance (R_{ct}) and electrochemical resistance (R_s) of the electrodes were analyzed (Table 1). The low conductivity of ZnO/Co_3O_4@350 could be attributed to its undeveloped crystallinity at low calcination temperatures. The relatively high R_{ct} of ZnO/Co_3O_4@550 could be due to defects in the nanosheets, as

https://doi.org/10.1021/acsomega.1c02059
ACS Omega 2021, 6, 23750−23763

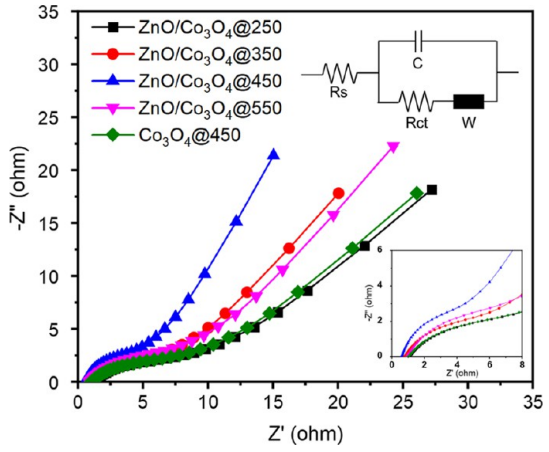

Figure 11. EIS measurements of Co_3O_4 and ZnO/Co_3O_4 calcined at different temperatures. The inset circuit is the equivalent circuit used for the EIS data analysis.

Table 1. Charge Transfer Resistance (R_{Ct}) and Electrochemical Resistance (R_s) of the Different Electrodes

electrode	R_{ct} (Ω)	R_s (Ω)
ZnO/Co_3O_4@250	2.827	1.025
ZnO/Co_3O_4@350	2.454	0.873
ZnO/Co_3O_4@450	2.324	0.578
ZnO/Co_3O_4@550	2.756	0.932
Co_3O_4@450	2.873	0.974

shown in Figure 2. The highest R_{ct} of Co_3O_4@450 could be explained by the lack of ZnO, which provided the electron pathway in the nanocomposite film.[68] On the other hand, the Z′-intercept represented the electrochemical resistance (R_s), which included the ionic resistance of the electrolyte, the intrinsic resistance of the active materials, and the contact resistance between the current collectors and the active materials. The lowest R_s of ZnO/Co_3O_4@450 was consistent with its well-developed nanosheets that had a high aspect ratio, and thus provided a large surface area to contact with the electrolyte. In contrast, Co_3O_4@450 had thick walls to limit the surface area for ion adsorption/desorption, as mentioned above.

In the low-frequency region, ZnO/Co_3O_4@450 exhibited a more inclined line than the others. This suggests that the intricate structure of ZnO/Co_3O_4@450 limited ion diffusion compared to the rapid ion adsorption/desorption on its large surface.[69,70]

Thus, the ZnO/Co_3O_4@450 nanocomposite deposited by the two-step CBD method was found to be a promising material for pseudocapacitors, and the importance of calcination temperature to develop crystalline structures was confirmed.

Finally, the cycle stability of ZnO/Co_3O_4 calcined at different temperatures and $ZnO@Co_3O_4$@450 were evaluated (Figure 12a).

The cycle stability was tested using GCD for 1000 cycles at a current density of 3.75 F g^{-1}. After 1000 cycles, the capacitance retention of ZnO/Co_3O_4@250, ZnO/Co_3O_4@350, ZnO/Co_3O_4@450, ZnO/Co_3O_4@550, and $ZnO@Co_3O_4$@450 were 78.7, 83.0, 85.7, 80.2, and 74.2%, respectively (Figure 12a). ZnO/Co_3O_4@450 indicated the highest stability and specific capacitance in this work. Table 2 shows the comparisons of the specific capacitance and stability of this work with previously reported Co_3O_4 nanocomposite electrodes. Although electrodes with excellent stability often have a propensity for less specific capacitance, both the specific capacitance and stability of the electrode in this work were good and even greater than those of some of the previously reported electrodes. The GCD measurements of electrodes were also conducted after the stability test at a current density of 3.64 A g^{-1} (Figure 12b). The sharp potential drop of the initial discharge (iR_{drop}) approximately indicates the internal resistance of the material and were in the order of ZnO/Co_3O_4@450 (53.7 mV) < ZnO/Co_3O_4@350 (75.8 mV) < ZnO/Co_3O_4@550 (90.1 mV) <ZnO/Co_3O_4@250 (98.8 mV) < $ZnO@Co_3O_4$@450 (105.6 mV). The iR_{drop} of ZnO/Co_3O_4@450 was considerably lower than those of the others, which suggests that ZnO/Co_3O_4@450 was more steadily bound to the Ni foam than the others in the charge/discharge cycles. The electrode with a lower internal resistance is crucial in energy storage to decrease unwanted energy loss and heat generation during charge/discharge processes. Thus, ZnO/Co_3O_4@450 exhibited the highest properties for the cycle stability.

The EIS spectra of ZnO/Co_3O_4@450 before and after the cyclic test were also analyzed with a Nyquist plot (Figure 12c). ZnO/Co_3O_4@450 exhibited a small increase in both R_s (from 0.578 to 0.653 Ω) and R_{ct} (from 2.324 to 2.457 Ω), which was most likely due to the mechanical stress during the repetitive charge−discharge process at a high current density.[76] Since the

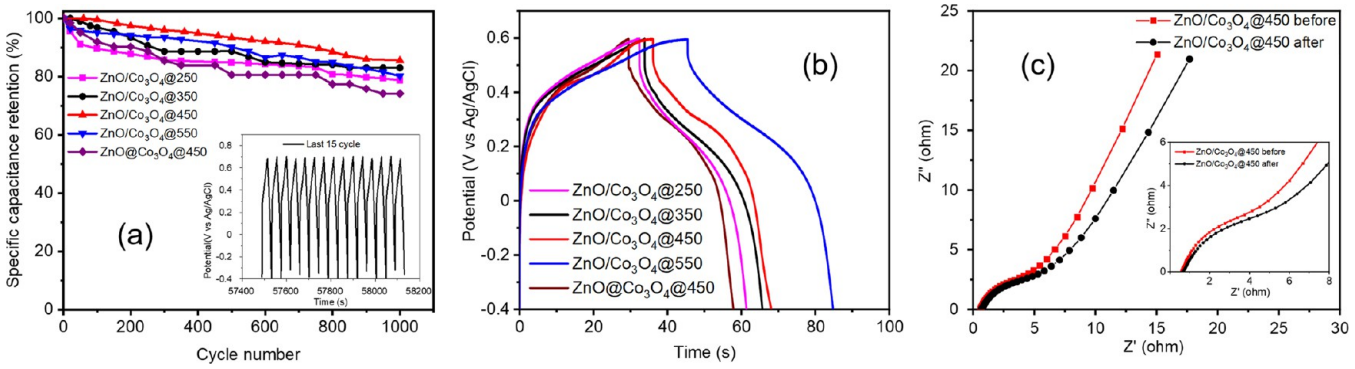

Figure 12. (a) Capacitance retention of ZnO/Co_3O_4 and $ZnO@Co_3O_4$ nanocomposites against cycle numbers with the GCD curves of the last 15 charge/discharge cycles of ZnO/Co_3O_4@450 (inset), (b) GCD curves of different nanocomposites after the stability test, and (c) the Nyquist plots of ZnO/Co_3O_4@450 before and after 1000 cycles.

https://doi.org/10.1021/acsomega.1c02059
ACS Omega 2021, 6, 23750−23763

Table 2. Comparison of the Specific Capacitance and Stability of Co Oxide Nanocomposites

electrode material	specific capacitance	stability	reference
ZnO/Co_3O_4 nanocomposite (ZnO/Co_3O_4@450)	940 F g^{-1} at 5 mV s^{-1} 690 F g^{-1} at 1 A g^{-1}	85.7% at 3.75 F g^{-1} after 1000 cycles	this work
Co_3O_4 nanoplate/graphene sheet	337.8 F g^{-1} at 0.2 A g^{-1}	93.2% at 1 A g^{-1} after 1000 cycle	71
$NiO-Co_3O_4$ composite	801 F g^{-1} at 1 A g^{-1}	85% at 8 A g^{-1} after 1000 cycle	72
rGO/Co_3O_4 composite	472 F g^{-1} at 2 mV s^{-1}	95.6% at 2 A g^{-1} after 1000 cycle	73
$MnO_2-Co_3O_4$ composite	605 F g^{-1} at 2 mV s^{-1}	55.6% at 100 mV s^{-1} after 1000 cycle	74
Core–double-shell $ZnO/ZnS@Co_3O_4$ heterostructure	777 F g^{-1} at 0.5 A g^{-1}	75% at 5 A g^{-1} after 3000 cycle	75

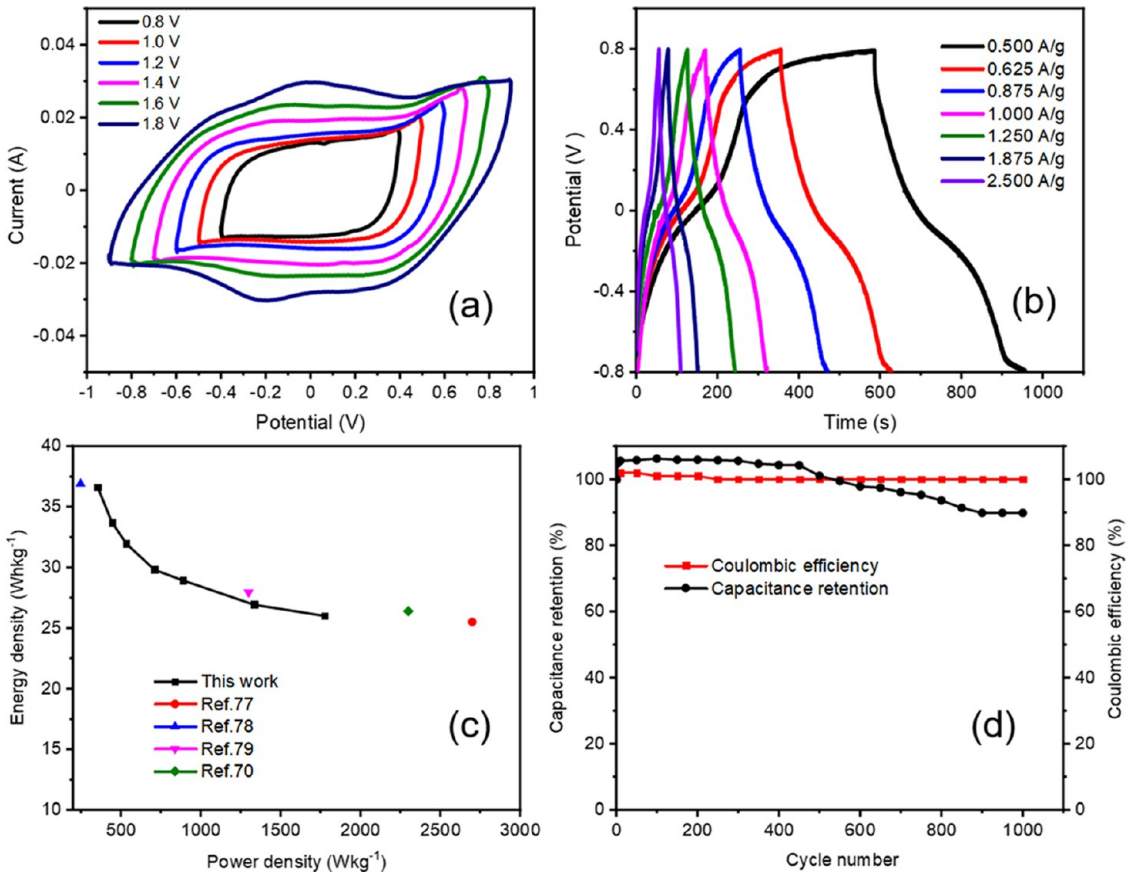

Figure 13. Electrochemical performance of the symmetric supercapacitor using ZnO/Co_3O_4@450 nanocomposites: (a) CV, (b) GCD, (c) Ragone plots compared with reported data, and (d) cycle stability and the Coulombic efficiency test at 6.67 A g^{-1}.

ZnO/Co_3O_4 nanocomposites were prepared without a binder, they were mechanically brittle. To improve their mechanical stability, these metal oxide nanocomposites could be sealed by other materials, such as gel electrolytes.

Electrochemical Performance of Symmetrical Systems. Considering practical applications, the ZnO/Co_3O_4@450 nanocomposite electrode was symmetrically assembled in the electrolyte of 1 M KOH. The CV was measured in various potential ranges (from −0.4/0.4 to −0.9/0.9 V) at a rate of 50 mV s^{-1} (Figure 13a). As the potential range extended, the shape of the CV curves changed from the quasi-rectangular shape to a more corrugated one with a larger area. This change indicates that the wider potential range resulted in the pseudocapacitive mechanism in the energy storage, besides the EDLC mechanism. Considering the electrolysis of water, which was found at 1.8 V, the potential range for this system could be 1.6 V (i.e., scanned from −0.8 to 0.8 V). The GCD measurements were also conducted using different current densities (Figure 13b). At all current densities, the GCD curve possessed a distinct plateau as the pseudocapacitive behavior was intensified by the symmetric configuration. The gravimetric capacitance decreased from 412 Fg^{-1} at a current density of 0.5 A g^{-1} as the current density increased to 2.5 A g^{-1}. The balance of the energy density and the power density was on the same curve with the other supercapacitors previously reported (Figure 13c):[77−80] the maximum energy density was 36.6 Wh kg^{-1} at a power density of 356 W kg^{-1}. The cycle life of the symmetric device was also tested for 1000 cycles at a high current density of 6.67 F g^{-1} (Figure 13d). The capacitance retention rate was 89.8% of the initial capacitance after the cycles, and an excellent Coulombic efficiency of 99.6%, which indicated the high reversibility of the ZnO/Co_3O_4@450 nanocomposite electrode.

CONCLUSIONS

In this study, we demonstrated a simple CBD method to prepare ZnO/Co_3O_4 nanocomposites directly on Ni foam for use as active materials in pseudocapacitors. The porous structures of ZnO/Co_3O_4, consisting of flat nanosheets, were easily obtained by the two-step CBD method of ZnO and

https://doi.org/10.1021/acsomega.1c02059
ACS Omega 2021, 6, 23750−23763

Co_3O_4. The predeposition of ZnO improved the aspect ratio of the Co_3O_4 nanosheets, while the one-step CBD method from the precursor mixture resulted in a disordered nanocomposite. The connected nanosheets provided suitable electroactive sites for electrolyte diffusion and pathways for charge transportation to improve the energy storage performance of the electrode. The calcination temperature was a critical factor for improving the capacitive performance of this nanocomposite, and the treatment at 450 °C resulted in the highest performance. The specific capacitance of ZnO/Co_3O_4 was 940 F g^{-1}, which was calculated from the CV curve at a scan rate of 5 mV s^{-1}, while the specific capacity of ZnO/Co_3O_4 was 740 F g^{-1} from the GCD curve at a current density of 0.75 A g^{-1}. Moreover, the ZnO/Co_3O_4 nanocomposite calcined at 450 °C showed sufficient cycling performance, where ∼85% of the capacitance was retained after 1000 cycles. Considering practical applications, a symmetric supercapacitor using two ZnO/Co_3O_4@450 electrodes was also examined in an aqueous system (1 M KOH). The pseudocapacitive behavior increased as the potential window extended, and the high energy density of 36.6 Wh kg^{-1} at a power density of 356 W kg^{-1} was demonstrated in a potential window of 1.6 V. After 1000 cycles, the symmetric system exhibited a high cycle stability of 89.8% with an excellent Coulombic efficiency of 99.6% despite the lack of a binder. These high electrochemical performances were due to the nanocomposite structures with a large surface area and high electrical conductivity, which were accomplished by the two-step CBD method of ZnO and Co_3O_4 and calcination at the proper temperature. Therefore, the binder-free ZnO/Co_3O_4 nanocomposites prepared by the simple two-step CBD method is a promising material for use in pseudocapacitors, and this method could be applied to other metal oxide nanocomposites.

MATERIALS AND METHODS

Materials. Cobalt nitrate hexahydrate ($Co(NO_3)_2{\cdot}6H_2O$, Acros Organics), zinc acetate dihydrate ($Zn(CH_3COO)_2{\cdot}2H_2O$, Alfa Aesar), hexamethylenetetramine (HMTA, Alfa Aesar), ammonia (NH_3, 35% Fisher Chemical), urea ($(NH_2)_2CO$, Acros Organics), and potassium hydroxide (KOH, Fisher Chemical) were all of analytical grade and used without further purification. Prior to deposition, a Ni foam substrate (Fucell CO., LTD, a thickness of 1.7 mm, 110 ppi) was cut into 2 × 1 cm^2 pieces and ultrasonically cleaned in isopropanol ($CH_3CH(OH)CH_3$, Acros Organics) and then in water for 10 min each. Throughout the experiments, ultrapure water with a resistivity of 18.2 MΩcm (Yamato, Japan) was used.

Deposition of ZnO. Powders of $Zn(CH_3COO)_2{\cdot}2H_2O$ (25 mmol, 275 mg) and HMTA (25 mmol, 175 mg) were dissolved in 50 mL of water, and ammonium was added dropwise to adjust the pH of the solution approximately to 12. A well-cleaned Ni foam was soaked in the solution and heated at 90 °C for 1.5 h. After the solution was cooled to ambient temperature, the Ni foam was removed from the solution and washed with plenty of water to remove any residual salt. Subsequently, the obtained ZnO-coated Ni foam was dried in air at 200 °C for 1 h. The mass (m) of the active material was calculated by subtracting the weight of the Ni foam before and after deposition, which was also similarly used with the other nanocomposites.

Synthesis of ZnO/Co_3O_4. The nanocomposites of ZnO and Co_3O_4 synthesized by the two-step bath deposition method (ZnO deposition and Co_3O_4 deposition) were named, ZnO/Co_3O_4. Powders of $Co(NO_3)_2{\cdot}6H_2O$ (65 mmol, 0.94 g) and urea (48 mmol, 0.144 g) were dissolved in 50 mL of water and stirred for 30 min to form a pink solution. The Ni foam coated with ZnO was immersed into the solution and kept at 90 °C for 1.5 h. After cooling to ambient temperature, the Ni foam was removed from the solution and cleaned with water several times. The Ni foam with the reaction product was treated at 200 °C for 1 h and then calcined at different temperatures of 250, 350, 450, and 550 °C for 1 h. For comparison, Co_3O_4 on a Ni foam without the predeposition of ZnO was also directly synthesized under the same conditions.

Synthesis of $ZnO@Co_3O_4$. The ZnO and Co_3O_4 nanocomposite was prepared by a one-step bath deposition method and named, $ZnO@Co_3O_4$. Powders of $Co(NO_3)_2{\cdot}6H_2O$ (65 mmol, 0.94 g), $Zn(CH_3COO)_2{\cdot}2H_2O$ (25 mmol, 275 mg), and urea (96 mmol, 0.288 g) were dissolved in water (50 mL) and stirred for 30 min to form a pink solution. A well-cleaned Ni foam was immersed in the precursor solution and heated at 90 °C for 1.5 h. After the solution was cooled to ambient temperature, the Ni foam was removed from the solution and washed with plenty of water to remove any residual salt. Thus, the obtained sample was dried in air at 200 °C for 1 h and calcined at 450 °C for 1 h.

Materials Characterization. Scanning electron microscopy (SEM) was conducted at an accelerating voltage of 10 kV to observe the morphology of the samples, and energy dispersive spectroscopy (EDS) was used to analyze the elemental compositions of the materials through the use of field emission scanning electron microscopy (FE-SEM; JEOL JSM-6500F). The crystalline structures of the ZnO/Co_3O_4 and Co_3O_4 nanocomposites were characterized using X-ray diffraction (XRD; Bruker D2 Phaser) with a Cu Kα radiation source (0.15418 nm) and a 2θ range of 10−80°. Fourier transform infrared (FTIR) absorption spectra were obtained by the transmission method using KBr pellets from 400−4000 cm^{-1} using absorption spectrometry (Nicolet Thermo Scientific 6700). The chemical status of samples was analyzed using X-ray photoelectron spectrometry (XPS, Auger electron microprobe (VG Scientific Microlab 350) with an EX05 ion gun (5 kV, maximum beam current >5 μA at 4 kV)).

Electrochemical Measurements. Cyclic voltammetry (CV) and galvanostatic charge/discharge (GCD) tests were performed to characterize the prepared electrodes using a three-electrode system with an electrochemical work station (CH1660E, Zahner CIMPS-X, xpot-26366) from −0.4 to 0.7 V (vs Ag/AgCl). Electrochemical impedance spectroscopy (EIS) measurements were carried out from 10 mHz to 100 kHz with a perturbation amplitude of 10 mV at the open-circuit potential. The specific capacitance was calculated from both the CV curve (C_{sc}) and the GCD curve (C_{sg}) using eqs 2 and 3, respectively[20]

$$C_{sc} = m^{-1}\nu^{-1}(V_f - V_i)^{-1}\int_{V_i}^{V_f} I(V)\mathrm{d}V \quad (2)$$

$$C_{sg} = I_g\Delta t m^{-1}(V_f - V_i)^{-1} \quad (3)$$

where m is the mass of the active material, ν is the scan rate, V_f and V_i are the final and initial potentials of the voltammetric curve, $I(V)$ is the voltammetric current, I_g is the given current, and Δt is the discharging time. During these electrochemical measurements, ZnO, ZnO/Co_3O_4, $ZnO@Co_3O_4$, and Co_3O_4

https://doi.org/10.1021/acsomega.1c02059
ACS Omega 2021, 6, 23750−23763

on Ni foam (area of 2 cm^2) acted as the working electrode. Ag/AgCl was used as the reference electrode, and a platinum wire acted as the counter electrode. For the symmetrical configuration, the nanocomposite was also used as the counter electrode. All electrochemical measurements were examined in an aqueous solution of KOH (1 M).

■ ASSOCIATED CONTENT

Supporting Information

The Supporting Information is available free of charge at https://pubs.acs.org/doi/10.1021/acsomega.1c02059.

SEM images and elemental mapping of ZnO/Co_3O_4@450 and survey XPS spectra of ZnO/Co_3O_4 nanocomposites and ZnO@Co_3O_4@450 (PDF)

■ AUTHOR INFORMATION

Corresponding Author

Masaki Ujihara − *Graduate Institute of Applied Science and Technology, National Taiwan University of Science and Technology, Taipei 10607 Taiwan, Republic of China;* orcid.org/0000-0003-2961-413X; Email: masaki.ujihara@mail.ntust.edu.tw

Author

Eshetu M. Abebe − *Graduate Institute of Applied Science and Technology, National Taiwan University of Science and Technology, Taipei 10607 Taiwan, Republic of China*

Complete contact information is available at: https://pubs.acs.org/10.1021/acsomega.1c02059

Notes

The authors declare no competing financial interest.

■ ACKNOWLEDGMENTS

This investigation was partly supported by Ministry of Science and Technology of the Republic of China, [MOST 109-2221-E-011-062], and Graduate Institute of Applied Science and Technology, National Taiwan University of Science and Technology.

■ REFERENCES

(1) Owusu, P. A.; Asumadu-Sarkodie, S. A review of renewable energy sources, sustainability issues and climate change mitigation. *Cogent Eng.* **2016**, *3*, No. 1167990.

(2) Liang, Z.; Zhao, R.; Qiu, T.; Zou, R.; Xu, Q. Metal-organic framework-derived materials for electrochemical energy applications. *EnergyChem* **2019**, *1*, No. 100001.

(3) Wang, C.; Li, X.; Li, Q.; Pang, H. Graphene/Co_3O_4 composites in application of electrochemical energy conversion and storage. *FlatChem* **2019**, *16*, No. 100107.

(4) Zhong, W.; Huang, X.; Lin, Y.; Cao, Y.; Wang, Z. Compact Co_3O_4/Co in-situ nanocomposites prepared by pulsed laser sintering as anode materials for lithium-ion batteries. *J. Energy chem.* **2021**, *58*, 386−390.

(5) Zhong, W.; Xiao, B.; Lin, Z.; Wang, Z.; Huang, L.; Shen, S.; Zhang, Q.; Gu, L. $RhSe_2$: a superior 3D electrocatalyst with multiple active facets for hydrogen evolution reaction in both acid and alkaline solutions. *Adv. Mater.* **2021**, *33*, No. 2007894.

(6) Zhong, W.; Wang, Z.; Gao, N.; Huang, L.; Lin, Z.; Liu, Y.; Meng, F.; Deng, J.; Jin, S.; Zhang, Q.; Gu, L. Coupled vacancy pairs in Ni-doped CoSe for improved electrocatalytic hydrogen production through topochemical deintercalation. *Angew. Chem., Int. Ed.* **2020**, *59*, 22743−22748.

(7) Shen, S.; Lin, Z.; Song, K.; Wang, Z.; Huang, L.; Yan, L.; Meng, F.; Zhang, Q.; Gu, L.; Zhong, W. Reversed active sites boost the intrinsic activity of graphene-like cobalt selenide for hydrogen evolution. *Angew. Chem., Int. Ed.* **2021**, *60*, 12360−12365.

(8) Wang, Z.; Lin, Z.; Deng, J.; Shen, S.; Meng, F.; Zhang, J.; Zhang, Q.; Zhong, W.; Gu, L. Oxygen evolution reaction: elevating the d-band center of six-coordinated octahedrons in Co_9S_8 through Fe-incorporated topochemical deintercalation. *Adv. Energy Mater* **2021**, *11*, No. 2170020.

(9) Lin, Z.; Shen, S.; Wang, Z.; Zhong, W. Laser ablation in air and its application in catalytic water Splitting and Li-ion battery. *iScience* **2021**, *24*, No. 102469.

(10) Stoller, M. D.; Park, S.; Zhu, Y.; An, J.; Ruoff, R. S. Graphene-based ultracapacitors. *Nano Lett.* **2008**, *8*, 3498−3502.

(11) Luo, G.; Huang, H.; Lei, C.; Cheng, Z.; Wu, X.; Tang, S.; Du, Y. Facile synthesis of porous graphene as binder-free electrode for supercapacitor application. *Appl. Surf. Sci.* **2016**, *366*, 46−52.

(12) Jang, G.-S.; Ameen, S.; Akhtar, M. S.; Kim, E.; Shin, H.-S. Electrochemical investigations of hydrothermally synthesized porous cobalt oxide (Co_3O_4) Nanorods: supercapacitor application. *ChemistrySelect* **2017**, *2*, 8941−8949.

(13) Xia, H.; Zhu, D.; Luo, Z.; Yu, Y.; Shi, X.; Yuan, G.; Xie, J. Hierarchically structured Co_3O_4@Pt@MnO_2 nanowire arrays for high-performance supercapacitors. *Sci. Rep.* **2013**, *3*, No. 2978.

(14) Fite, M. C.; Rao, J.-Y.; Imae, T. Effect of external magnetic field on hybrid supercapacitors of nitrogen-doped graphene with magnetic metal oxides. *Bull. Chem. Soc. Jpn.* **2020**, *93*, 1139−1149.

(15) Debelo, T. T.; Ujihara, M. Effect of simultaneous electrochemical deposition of manganese hydroxide and polypyrrole on structure and capacitive behavior. *J. Electroanal. Chem.* **2020**, *859*, No. 113825.

(16) Iro, Z. S.; Subramani, C.; Dash, S. S. A brief review on electrode materials for supercapacitor. *Int. J. Electrochem. Sci.* **2016**, 10628−10643.

(17) Simon, P.; Gogotsi, Y. Materials for electrochemical capacitors. *Nat. Mater.* **2008**, *7*, 845−854.

(18) Gao, M.; Wang, W.-K.; Rong, Q.; Jiang, J.; Zhang, Y.-J.; Yu, H.-Q. Porous ZnO-coated Co_3O_4 nanorod as a high-energy-density supercapacitor material. *ACS Appl. Mater. Interfaces* **2018**, *10*, 23163−23173.

(19) Cai, D.; Huang, H.; Wang, D.; Liu, B.; Wang, L.; Liu, Y.; Li, Q.; Wang, T. High-performance supercapacitor electrode based on the unique ZnO@Co_3O_4 core/shell heterostructures on nickel foam. *ACS Appl. Mater. Interfaces* **2014**, *6*, 15905−15912.

(20) Li, H.; Wang, R.; Cao, R. Physical and electrochemical characterization of hydrous ruthenium oxide/ordered mesoporous carbon composites as supercapacitor. *Microporous Mesoporous Mater.* **2008**, *111*, 32−38.

(21) Liu, X.; Chen, G.; Guan, H.; Dong, C.; Xiao, X.; Wang, Y. Binder-free NiO@MnO_2 core-shell electrode: rod-like NiO core prepared through corrosion by oxalic acid and enhanced pseudocapacitance with sphere-like MnO_2 shell. *Electrochim. Acta* **2016**, *189*, 83−92.

(22) Li, X.; Jiang, L.; Zhou, C.; Liu, J.; Zeng, H. Integrating large specific surface area and High conductivity in hydrogenated $NiCo_2O_4$ double-shell hollow spheres to improve supercapacitors. *NPG Asia Mater.* **2015**, *7*, No. e165.

(23) Huang, Y.; Liang, J.; Chen, Y. An overview of the applications of graphene-based materials in supercapacitors. *Small* **2012**, *8*, 1805−1834.

(24) Zhang, L. L.; Zhao, X. S. Carbon-based materials as supercapacitor electrodes. *Chem. Soc. Rev.* **2009**, *38*, 2520−2531.

(25) Snook, G. A.; Kao, P.; Best, A. S. Conducting-polymer-based supercapacitor devices and electrodes. *J. Power Sources* **2011**, *196*, 1−12.

(26) Liu, Y.; Gao, C.; Li, Q.; Pang, H. Nickel oxide/graphene composites: synthesis and applications. *Chem. Eur. J,* **2019**, *25*, 2141−2160.

(27) Hu, C.-C.; Chang, K.-H.; Lin, M.-C.; Wu, Y.-T. Design and tailoring of the nanotubular arrayed architecture of hydrous RuO_2 for next generation supercapacitors. *Nano Lett.* **2006**, *6*, 2690−2695.
(28) Wang, Y.; Song, Y.; Xia, Y. Electrochemical capacitors: mechanism, materials, systems, characterization and applications. *Chem. Soc. Rev.* **2016**, *45*, 5925−5950.
(29) Tajik, S.; Dubal, D. P.; Gomez-Romero, P.; Yadegari, A.; Rashidi, A.; Nasernejad, B.; Inamuddin; Asiri, A. M. Nanostructured mixed transition metal oxides for high performance asymmetric supercapacitors: facile synthetic strategy. *Int. J. Hydrogen Energy* **2017**, *42*, 12384−12395.
(30) Hai, Z.; Karbalaei Akbari, M.; Xue, C.; Xu, H.; Solano, E.; Detavernier, C.; Hu, J.; Zhuiykov, S. Atomically-thin WO_3/TiO_2 heterojunction for supercapacitor electrodes developed by atomic layer deposition. *Compos. Commun.* **2017**, *5*, 31−35.
(31) Yan, Y.; Li, K.; Chen, X.; Yang, Y.; Lee, J.-M. Heterojunction-assisted $Co_3S_4@Co_3O_4$ core−shell octahedrons for supercapacitors and both oxygen and carbon dioxide reduction reactions. *Small* **2017**, *13*, No. 1701724.
(32) Pang, H.; Ma, Y.; Li, G.; Chen, J.; Zhang, J.; Zheng, H.; Du, W. Facile synthesis of porous ZnO−NiO composite micropolyhedrons and their application for high power supercapacitor electrode materials. *Dalton Trans.* **2012**, *41*, 13284−13291.
(33) Wang, L.; Guan, Y.; Zhao, X.; Mu, J.; Che, H.; Li, H.; Guo, Z. $ZnCo_2O_4@MnCo_2O_4$ heterojunction structured nanosheets for high-performance supercapacitor. *J. Mater. Sci. Mater. Electron.* **2018**, *29*, 5782−5790.
(34) Wang, K.-B.; Xun, Q.; Zhang, Q. Recent progress in metal-organic frameworks as active materials for supercapacitors. *EnergyChem* **2020**, *2*, No. 100025.
(35) Li, Y.; Shan, Y.; Pang, H. Design and synthesis of nitrogen-doped hexagonal NiCoO nanoplates derived from Ni-Co-MOF for high-performance electrochemical energy storage. *Chin. Chem. lett.* **2020**, *31*, 2280−2286.
(36) Guo, C.; Yin, M.; Wu, C.; Li, J.; Sun, C.; Jia, C.; Li, T.; Hou, L.; Wei, Y. Highly stable gully-network Co_3O_4 nanowire arrays as battery-type electrode for outstanding supercapacitor performance. *Front. Chem.*, **2018**, *6*, No. 636.
(37) Li, X.; Wang, J.; Ge, F.; Komarneni, S.; Cai, Z. Facile fabrication of freestanding three-dimensional composites for supercapacitors. *Chem. Commun.* **2016**, *52*, 2691−2694.
(38) He, Y.-B.; Li, G.-R.; Wang, Z.-L.; Su, C.-Y.; Tong, Y.-X. Single-crystal ZnO nanorod/amorphous and nanoporous metal oxide shell composites: controllable electrochemical synthesis and enhanced supercapacitor performances. *Energy Environ. Sci.* **2011**, *4*, 1288−1292.
(39) Radhamani, A. V.; Shareef, K. M.; Rao, M. S. R. $ZnO@MnO_2$ core−shell nanofiber cathodes for high performance asymmetric supercapacitors. *ACS Appl. Mater. Interfaces* **2016**, *8*, 30531−30542.
(40) Wang, Y.; He, J.; Roller, J.; Maric, R. One-step fabrication of binder-free three-dimensional Co_3O_4 electrodes by reactive spray deposition technology for application in high-performance supercapacitors. *MRS Commun.* **2018**, *8*, 597−603.
(41) Zhong, J.-H.; Wang, A.-L.; Li, G.-R.; Wang, J.-W.; Ou, Y.-N.; Tong, Y.-X. $Co_3O_4/Ni(OH)_2$ composite mesoporous nanosheet networks as a promising electrode for supercapacitor applications. *J. Mater. Chem.* **2012**, *22*, 5656−5665.
(42) Chen, Q.; Lei, S.; Deng, P.; Ou, X.; Chen, L.; Wang, W.; Xiao, Y.; Cheng, B. Direct growth of nickel terephthalate on Ni foam with large mass-loading for high-performance supercapacitors. *J. Mater. Chem. A* **2017**, *5*, 19323−19332.
(43) Yang, G.-W.; Xu, C.-L.; Li, H.-L. Electrodeposited nickel hydroxide on nickel foam with ultrahigh capacitance. *Chem. Commun.* **2008**, 6537−6539.
(44) Baviskar, P. K.; Nikam, P. R.; Gargote, S. S.; Ennaoui, A.; Sankapal, B. R. Controlled synthesis of ZnO nanostructures with assorted morphologies via simple solution chemistry. *J. Alloys Compd.* **2013**, *551*, 233−242.
(45) Dalache, C.; Benhebal, H.; Benrabah, B.; Ammari, A.; Kharroubi, A.; Lakhal, A. Cadmium-doped Co_3O_4 thin films: synthesis and characterization. *Surf. Rev. Lett.* **2019**, *26*, No. 1850134.
(46) Abdelmohsen, A.; Ismail, N. Morphology transition of ZnO and Cu_2O nanoparticles to 1D, 2D, and 3D nanostructures: hypothesis for engineering of micro and nanostructures (HEMNS). *J. Sol-gel Sci. Technol.* **2020**, 213−228.
(47) Abdelmohsen, A. H.; Rouby, W. M. A. E.; Ismail, N.; Farghali, A. A. Morphology transition engineering of ZnO nanorods to nanoplatelets grafted Mo_8O_{23}-MoO_2 by polyoxometalates: mechanism and possible applicability to other Oxides. *Sci. Rep.* **2017**, *7*, No. 5946.
(48) Shin, J. W.; Lee, J. Y.; Kim, T. W.; No, Y. S.; Cho, W. J.; Choi, W. K. Growth mechanisms of thin-film columnar structures in zinc oxide on p-type Silicon Substrates. *Appl. Phys. Lett.* **2006**, *88*, No. 091911.
(49) Peiró, A. M.; Ravirajan, P.; Govender, K.; Boyle, D. S.; O'Brien, P.; Bradley, D. D.; Nelson, J. Hybrid polymer/metal oxide solar cells based on ZnO columnar structures. *J. Mater. Chem.* **2006**, *16*, 2088−2096.
(50) Yang, Q.; Lu, Z.; Sun, X.; Liu, J. Ultrathin Co_3O_4 nanosheet arrays with high supercapacitive performance. *Sci. Rep.* **2013**, *3*, No. 3537.
(51) Han, X.; Wahl, S.; Russo, P. A.; Pinna, N. Cobalt-assisted morphology and assembly control of Co-doped ZnO nanoparticles. *Nanomaterials* **2018**, *8*, No. 249.
(52) Liu, M.; Chang, J.; Sun, J.; Gao, L. Synthesis of porous NiO using NaBH4 dissolved in ethylene glycol as precipitant for high-performance supercapacitor. *Electrochim. Acta* **2013**, *107*, 9−15.
(53) Ali, F.; Khalid, N. R. Effect of calcination temperature on structural, morphological and electrochemical properties of Sn doped Co_3O_4 nanorods. *Ceram. Int.* **2020**, *46*, 24137−24146.
(54) Khavale, S. V.; Lokhande, B. J. Electrochemical performance of potentio-dynamically deposited Co_3O_4 electrodes: influence of annealing temperature. *J. Mater. Sci. Mater. Electron.* **2017**, *28*, 5106−5115.
(55) Geleta, T. A.; Imae, T. Influence of additives on zinc oxide-based dye sensitized solar cells. *Bull. Chem. Soc. Jpn.* **2020**, *93*, 611−620.
(56) Liu, F.; Su, H.; Jin, L.; Zhang, H.; Chu, X.; Yang, W. Facile synthesis of ultrafine cobalt oxide nanoparticles for high-performance supercapacitors. *J. Colloid Interface Sci.* **2017**, *505*, 796−804.
(57) Xia, X.-h.; Tu, J.-p.; Mai, Y.-j.; Wang, X.-l.; Gu, C.-d.; Zhao, X.-b. Self-supported hydrothermal synthesized hollow Co_3O_4 nanowire arrays with high supercapacitor capacitance. *J. Mater. Chem.* **2011**, *21*, 9319−9325.
(58) Huang, M.; Zhang, Y.; li, F.; Zhang, L.; Ruoff, R.; Wen, Z.; Liu, Q. Self-sssembly of mesoporous nanotubes assembled from interwoven ultrathin birnessite-type MnO_2 nanosheets for asymmetric Supercapacitors. *Sci. Rep.* **2015**, *4*, No. 3878.
(59) Liu, Y.; Zhu, G.; Ge, B.; Zhou, H.; Yuan, A.; Shen, X. Concave Co_3O_4 octahedral mesocrystal: polymer-mediated synthesis and sensing properties. *CrystEngComm* **2012**, *14*, 6264−6270.
(60) Xu, H.; Shi, M.; Liang, C.; Wang, S.; Xia, C.; Xue, C.; Hai, Z.; Zhuiykov, S. Effect of zinc acetate concentration on optimization of photocatalytic activity of p-Co_3O_4/n-ZnO heterostructures. *Nanoscale Res. Lett.* **2018**, *13*, No. 195.
(61) Panigrahy, B.; Aslam, M.; Bahadur, D. Aqueous synthesis of Mn- and Co-Doped ZnO nanorods. *J. Phys. Chem. C* **2010**, *114*, 11758−11763.
(62) Kalasina, S.; Phattharasupakun, N.; Wutthiprom, J.; Promarak, V.; Sudyoadsuk, T.; Sawangphruk, M. A Single energy conversion and storage device of cobalt oxide nanosheets and N-doped reduced rraphene oxide aerogel. *ECS Trans.* **2018**, *85*, 435−447.
(63) Dupin, J.-C.; Gonbeau, D.; Vinatier, P.; Levasseur, A. Systematic XPS studies of metal oxides, hydroxides and peroxides. *Phys. Chem. Chem. Phys.* **2000**, *2*, 1319−1324.

https://doi.org/10.1021/acsomega.1c02059
ACS Omega 2021, 6, 23750−23763

(64) Alnoor, H.; Savoyant, A.; Liu, X.; Pozina, G.; Willander, M.; Nur, O. An effective low-temperature solution synthesis of Co-doped [0001]-oriented ZnO nanorods. *J. Appl. phys.* **2017**, *121*, No. 215102.
(65) Gholamvand, Z.; McAteer, D.; Harvey, A.; Backes, C.; Coleman, J. N. Electrochemical applications of two-dimensional nanosheets: the effect of nanosheet length and thickness. *Chem. Mater.* **2016**, *28*, 2641−2651.
(66) Li, W.; Wang, X.; Hu, Y.; Sun, L.; Gao, C.; Zhang, C.; Liu, H.; Duan, M. Hydrothermal synthesized of CoMoO(4) microspheres as excellent electrode material for supercapacitor. *Nanoscale Res. Lett* **2018**, *13*, No. 120.
(67) Liao, Q.; Li, N.; Jin, S.; Yang, G.; Wang, C. All-solid-state symmetric supercapacitor based on Co_3O_4 nanoparticles on vertically aligned graphene. *ACS Nano* **2015**, *9*, 5310−5317.
(68) Hu, N.; Gong, W. H.; Huang, L.; Shen, P. K. Ultrahigh energy density asymmetric electrochemical capacitors based on flower-like ZnO/Co_3O_4 nanobundle arrays and stereotaxically constricted graphene. *J. Mater. Chem. A* **2019**, *7*, 1273−1280.
(69) Shi, B.; Saravanakumar, B.; Wei, W.; Dong, G.; Wu, S.; Lu, X.; Zeng, M.; Gao, X.; Wang, Q.; Zhou, G.; Liu, J.-M.; Kempa, K.; Gao, J. 3D honeycomb $NiCo_2S_4$ @ $Ni(OH)_2$ nanosheets for flexible all-solid-state asymmetric supercapacitors with enhanced specific capacitance. *J. Alloys Compd.* **2019**, *790*, 693−702.
(70) Chong, B. M.; Azman, N. H. N.; Mohd Abdah, M. A. A.; Sulaiman, Y. Supercapacitive performance of N-doped graphene/Mn_3O_4/Fe_3O_4 as an electrode material. *Appl. Sci.* **2019**, *9*, No. 1040.
(71) Wang, L.; Wang, D.; Zhu, J.; Liang, X. Preparation of Co_3O_4 nanoplate/graphene sheet composites and their synergistic electrochemical performance. *Ionics* **2013**, *19*, 215−220.
(72) Wang, X. W.; Zheng, D. L.; Yang, P. Z.; Wang, X. E.; Zhu, Q. Q.; Ma, P. F.; Sun, L. Y. Preparation and electrochemical properties of NiO-Co_3O_4 composite as electrode materials for supercapacitors. *Chem. Phys. Lett.* **2017**, *667*, 260−266.
(73) Xiang, C.; Li, M.; Zhi, M.; Manivannan, A.; Wu, N. A reduced graphene oxide/Co_3O_4 composite for supercapacitor electrode. *J. Power Sources* **2013**, *226*, 65−70.
(74) Khavale, S. V.; Ambare, R. C.; Lokhande, B. J. Molar optimization of MnO_2 to form composite with Co_3O_4 by potentiodynamic electrodeposition for better electrochemical characterizations. *J. Mater. Sci. Mater. Electron.* **2020**, *31*, 7315−7323.
(75) Sarkar, S.; Maiti, S.; Mahanty, S.; Basak, D. Core-double shell ZnO/ZnS@Co_3O_4 heterostructure as high performance pseudocapacitor. *Dalton Trans.* **2016**, *45*, 9103−9112.
(76) Xiao, M.; Su, Y.; Zhao, M.; Du, B. Synthesis of CoTe nanowires: a new electrode material for supercapacitor with high stability and high performance. *Nanotechnology* **2019**, *31*, No. 055706.
(77) Sundriyal, S.; Shrivastav, V.; Kaur, H.; Mishra, S.; Deep, A. high-performance symmetrical supercapacitor with a combination of a ZIF-67/rGO composite electrode and a redox additive electrolyte. *ACS Omega* **2018**, *3*, 17348−17358.
(78) Li, C.; Wu, W.; Wang, P.; Zhou, W.; Wang, J.; Chen, Y.; Fu, L.; Zhu, Y.; Wu, Y.; Huang, W. Fabricating an aqueous symmetric supercapacitor with a stable high working voltage of 2 V by using an alkaline−acidic electrolyte. *Adv. Sci.* **2019**, *6*, No. 1801665.
(79) Raphael Ezeigwe, E.; Dong, L.; Wang, J.; Wang, L.; Yan, W.; Zhang, J. MOF-deviated zinc-nickel−cobalt ZIF-67 electrode material for high-performance symmetrical coin-shaped supercapacitors. *J. Colloid Interface Sci.* **2020**, *574*, 140−151.
(80) Kumar, A.; Sanger, A.; Kumar, A.; Mishra, Y. K.; Chandra, R. Performance of high energy density symmetric supercapacitor based on sputtered MnO_2 nanorods. *ChemistrySelect* **2016**, *1*, 3885−3891.

https://doi.org/10.1021/acsomega.1c02059
ACS Omega 2021, 6, 23750−23763